HHS Public Access

Author manuscript

Cell Rep. Author manuscript; available in PMC 2023 January 16.

Published in final edited form as:

Cell Rep. 2022 December 27; 41(13): 111873. doi:10.1016/j.celrep.2022.111873.

Multi-modal characterization and simulation of human epileptic circuitry

Anatoly Buchin[1,10,*], **Rebecca de Frates**[1,12], **Anirban Nandi**[1,12], **Rusty Mann**[1], **Peter Chong**[1], **Lindsay Ng**[1], **Jeremy Miller**[1], **Rebecca Hodge**[1], **Brian Kalmbach**[1,2], **Soumita Bose**[1,3], **Ueli Rutishauser**[6,7,9], **Stephen McConoughey**[1,11], **Ed Lein**[1,5], **Jim Berg**[1], **Staci Sorensen**[1], **Ryder Gwinn**[4], **Christof Koch**[1], **Jonathan Ting**[1,5], **Costas A. Anastassiou**[1,6,7,8,9,13,*]

[1]Allen Institute for Brain Science, Seattle, WA, USA

[2]University of Washington, Seattle, WA, USA

[3]CiperHealth, San Francisco, CA, USA

[4]Swedish Medical Center, Seattle, WA, USA

[5]University of Washington, Seattle, WA, USA

[6]Department of Neurosurgery, Cedars-Sinai Medical Center, Los Angeles, CA 90048, USA

[7]Department of Neurology, Cedars-Sinai Medical Center, Los Angeles, CA 90048, USA

[8]Board of Governors Regenerative Medicine Institute, Cedars-Sinai Medical Center, Los Angeles, CA 90048, USA

[9]Center for Neural Science and Medicine, Department of Biomedical Sciences, Cedars-Sinai Medical Center, Los Angeles, CA 90048, USA

[10]Present address: Cajal Neuroscience, Inc., Seattle, WA, USA

[11]Present address: Institute for Advanced Clinical Trials for Children, 9200 Corporate Blvd, Suite 350, Rockville, MD 20850, USA

[12]These authors contributed equally

[13]Lead contact

SUMMARY

*Correspondence: anat.buchin@gmail.com (A.B.), costas.anastassiou@cshs.org (C.A.A.).

AUTHOR CONTRIBUTIONS

Conceptualization, C.A.A. and J.T.; data generation, A.B., A.N., R.d.F., P.C., R.M., B.K., R.G., S.B., J.T., and R.H.; data curation, J.B., C.A.A., J.T., R.d.F., S.M., and S.S.; formal analysis, A.B., R.d.F., and C.A.A.; funding acquisition, C.A.A., J.T., and C.K.; investigation, A.B., J.T., and C.A.A.; project administration, C.A.A., J.T., S.M., and C.K.; writing – original draft, A.B. and C.A.A.; writing – review and editing, all authors.

DECLARATION OF INTERESTS

The authors declare no competing interests.

SUPPLEMENTAL INFORMATION

Supplemental information can be found online at https://doi.org/10.1016/j.celrep.2022.111873.

Temporal lobe epilepsy is the fourth most common neurological disorder, with about 40% of patients not responding to pharmacological treatment. Increased cellular loss is linked to disease severity and pathological phenotypes such as heightened seizure propensity. While the hippocampus is the target of therapeutic interventions, the impact of the disease at the cellular level remains unclear. Here, we show that hippocampal granule cells change with disease progression as measured in living, resected hippocampal tissue excised from patients with epilepsy. We show that granule cells increase excitability and shorten response latency while also enlarging in cellular volume and spine density. Single-nucleus RNA sequencing combined with simulations ascribes the changes to three conductances: BK, Cav2.2, and Kir2.1. In a network model, we show that these changes related to disease progression bring the circuit into a more excitable state, while reversing them produces a less excitable, “early-disease-like” state.

In brief

The cellular changes brought about by temporal lobe epilepsy in humans remain unknown. Buchin et al. generate a multimodal dataset from human hippocampal surgical tissue to map cellular changes linked to disease progression. They find three ion conductances that explain changes across modalities.

Graphical Abstract

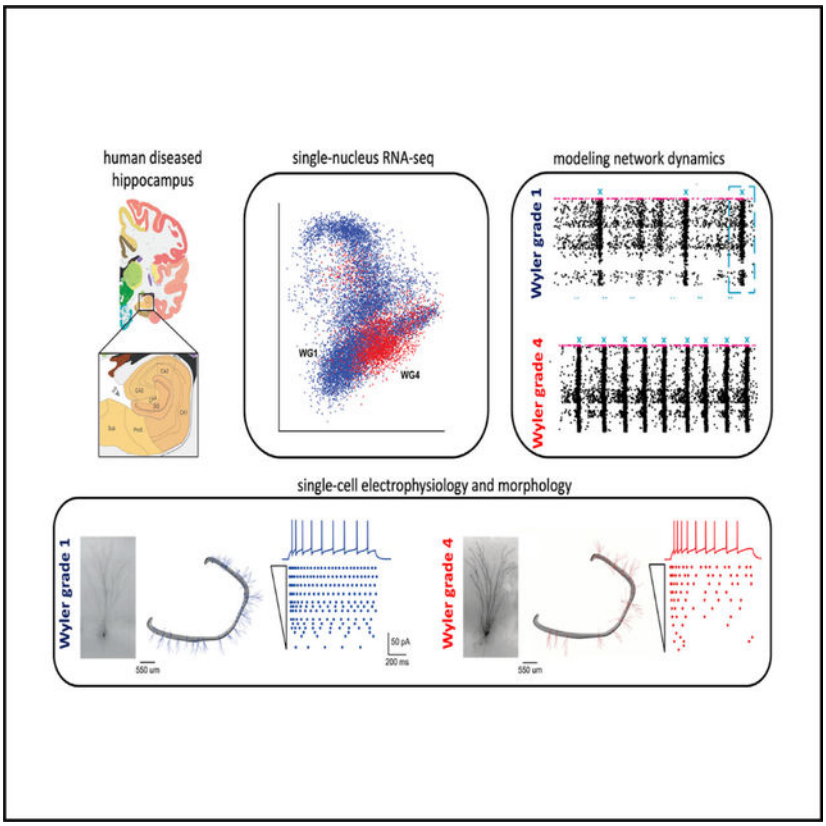

INTRODUCTION

Epilepsy is one of the most common neurologic ailments, and temporal lobe epilepsy (TLE) is its most commonly diagnosed form, affecting approximately 65 million people worldwide. Despite considerable advances in the diagnosis and treatment of such seizure disorders, the cellular and molecular mechanisms leading to TLE-related seizures remain unclear. Notably, approximately 40% of patients with TLE exhibit pharmaco-resistance, i.e., lack of response to conventional anticonvulsive treatments.[1] Hippocampal sclerosis (HS), a neuropathological condition correlated with cell loss and gliosis, has been linked to increased occurrence of TLE, with an elevated degree of HS contributing to the disease progression (though other factors like seizure duration may also affect it, e.g., see Fuerst et al.[2]). The sclerotic hippocampus is thought to be the most likely origin of chronic seizures in patients with TLE and is the target of temporal lobe resection intervention. The efficacy of these surgical interventions (i.e., 65%–80% of patients with TLE become seizure free) further implicates the sclerotic hippocampus as a prominent member of the pathophysiological network.[3,4] Patients with increased HS typically suffer from more frequent seizure activity,[5–9] an observation also replicated in rodents.[10] Furthermore, HS has been associated with a spectrum of adverse effects such as longer epilepsy duration[11–14] and an earlier stage of onset,[9,15,16] as well as the presence of early aberrant neurological insults such as febrile convulsions.[9,15,16]

To mechanistically understand the link between disease progression and increased seizure propensity in patients with TLE, we studied live human brain tissue excised during temporal lobectomy (Figure 1; Table S1). The excised brain tissue was quantified neuropathologically via the Wyler grade (WG; WG range: 1–4)[17] based on light microscopic examination of the mesial temporal damage in temporal lobectomy specimens (Figure 1A): degree 1 (WG1) corresponds to none/mild HS, while degree 3 or 4 (WG4) corresponds to severe HS. We use a data generation and analysis platform[18] to characterize disease-related features in gene expression (single-nucleus RNA sequencing [RNA-seq]), electrophysiology, morphology, spine density, and gene expression at single-cell resolution. Specifically, we concentrated on granule cells (GCs) of the dentate gyrus (DG), a hippocampal region. Studies in animal models and human neurosurgical specimens have implicated DG GCs in the generation and support of seizure activity by a plethora of mechanisms spanning from altered excitability, changes in morphology, protein expression, neuronal loss, synaptic re-organization, and altered connectivity patterns.[19–21] We pursued the multimodal characterization of human GCs across patients and report how their properties change with disease progression, i.e., increasing WG (Figures 1B, 1C, S1, and S2).

RESULTS

Single-cell gene expression changes in human GCs with TLE progression

To look at broad changes brought about by TLE in the human epileptic hippocampus, we analyzed the gene expression of 230 ion-channel-coding and 1,600 projection-coding genes specific to GCs (https://www.brainspan.org/; Figure 1B). Analysis of the single-nucleus RNA-seq (snRNA-seq) data after integration (https://scvi-tools.org/; see STAR Methods) shows that a large number of genes are differentially expressed with disease progression

that separates WG1 from WG4 GCs (Figure 1B). Differential expression implicates a large number of genes with the largest change (effect size) seen in FSTL4, GABRC3, EFNA5, and KCNC2 (Figure S3). FSTL4 is involved in cell differentiation; GABRG3 encodes the GABA-A receptor beta 3 subunit; EFNA5 is involved in cell migration during neuronal development; and KCNC2 is a potassium-channel-coding gene. In addition, we found that the proportion of GCs was larger in WG1 compared with WG4 patients (57% vs. 30% of all cells, respectively).

Transcriptomics broadly implicate a large number of GC-related genes to TLE progression. Thus, a number of GC properties change with disease progression in parallel to progressive cell loss in human hippocampus. To shed light into the cellular changes implicated by snRNA-seq as well as attribute these changes to specific mechanisms, we performed a single-cell electrophysiology and a morphology survey of GCs in human brain slices from the same patients and examined how these properties change with disease progression (Figures 1C and S3). The hypotheses for the mechanisms and the cellular changes affected by TLE progression are, thus, predominantly driven by the electrophysiology and morphology differences found in human GCs, with snRNA-seq used to further support changes we detect in the computational models related to ion-channel-related gene expression.

Excitability changes in GCs with TLE progression

We employed whole-cell patch clamping in human DG GCs, imposing a battery of intracellular stimuli to assess electrophysiological changes associated with HS. The standard protocol (1-s-long direct current [dc] injections of different amplitudes) was applied to 112 patch-clamped GCs (Figure 2A). A set of 31 electrophysiological features was extracted for every experiment (Table S2) and evaluated over the range of injected current amplitudes. Based on these electrophysiology features, we observed robust separation between WG1 and WG4 cases (Figures 2B and 2C; t-distributed stochastic neighbor embedding [t-SNE][22]). To identify the electrophysiology features separating WG1 vs. WG4, we used two methods: (1) pairwise feature comparison in combination with Mann-Whitney U testing ($p < 0.05/n$, Bonferroni corrected for multiple comparisons n), which resulted in 9 out of 30 features exhibiting statistically significant difference (Figure 2D); and (2) random forest classification reaching classification accuracy of 81% (chance level: 50%; classifier trained on all electrophysiological features; out-of-bag error; Figure 2E). When comparing the classifying features resulting from the two methods, we found that 5 out of 9 statistically significant features were shared (Figures 2D and 2E). The most prominent electrophysiological features affected by disease progression are the spike frequency-current (f-I) gain (WG1 GCs have a higher gain than WG4) and the time-to-spike (WG4 GCs have a shorter time-to-spike duration than WG1), two prominent excitability parameters of a neuron (Figure 2F). To cross-validate against patient-specific effects, patient-out-validation (classifier trained on data from 6 patients predicting the WG score of a seventh patient) classification performance reached 71% (chance level: 50%; Table S3).

Altered GC morphology and spine density

Next, we ask to what extent the morphology of human GCs is affected by disease progression. To do so, we reconstructed the dendritic morphology of 102 single GCs (Figure 3A) and used a set of 49 morphology features to assess WG-dependent alterations (Table S4). We found that morphologies differ between neurons from different levels of disease progression (Figures 3B and 3C) but are not clustered by patients (Figure S4). Following the same methodology as for electrophysiology features, we used two tests to detect the features leading to the morphology separation (Figures 3D and 3E). Random forest classification (out-of-bag error) resulted in a morphology-based classification performance of 74%, i.e., comparable to that of electrophysiology features. Notably, most features point to disease progression correlating with thicker (i.e., increased surface area and volume) GC morphologies. When training on both electrophysiological (Figure 2) and morphology features (Figure 3) for the subset of GCs (n = 77) where both data modalities are present, classifier performance reached 81% (Figure S5).

To what extent is synaptic input along GCs affected by disease progression? To determine the amount of excitatory synaptic input along GCs, we estimate the spine density in a subset of the morphological biocytin reconstructions (Figure 3F). Average spine density increases approximately 2-fold from WG1 to WG4. This suggests an increase in synaptic drive of GCs with disease progression. Notably, differences in spine density occurred both along the apical and basal dendrites. Overall, our results from spine density measurements indicate that DG GCs in severe stages of HS receive increased excitatory synaptic drive compared with mild HS.

Ion conductance changes

To investigate the functional consequences of TLE and HS on electrophysiological, morphological, and connectivity properties of human GCs, we generated a series of biophysically detailed, anatomically realistic, conductance-based single-neuron models.[23] To produce faithful single-neuron models, a key question is which ionic conductances to account for. Our starting point for the ionic conductance recipe relied on a detailed GC model based on the rodent literature that involves 7 voltage-dependent K channels, 4 voltage-dependent Ca channels, and 2 Ca-dependent K channels, as well as two voltage-dependent Na and Na/K (HCN) channels distributed along different parts of the morphology (Figure 4A; see also Beining et al.[24]). To assess to what extent these conductances are truly present in human GCs, in a second step, we analyzed fluorescence-activated cell-sorted snRNA-seq data from four human brain specimens[25] to test for the expression of genes associated with the ionic conductances used in our models. We found that the vast majority of the genes associated with the conductances are expressed in human DG neurons (Figure 4B).

To generate human GC single-neuron models, we used a 3-stage approach leveraging a computationally intensive, genetic optimization framework that relies on comparisons between experimental and model electrophysiology features for a particular morphology reconstruction (Figure S6). Using this optimization framework, we generated GC models accounting for active ionic conductances along their entire soma, axonal, and dendritic arbor.

In total, we developed 12 single-cell models per WG (data originating from multiple single cells and patients) in an unbiased manner. The resulting models captured a multitude of experimental observables such as differences between WG1 and WG4 in terms of spike frequency response to increasing injection currents, time to spike, etc. (Figures 4C and S7) As a result, when classifying electrophysiology features from these models, WG1 vs. WG4 models are clearly separated, and, importantly, the features leading to this separation are in agreement with the ones leading to separation of experimental electrophysiology features (Figures 4D and S7) (note that while the models were optimized on a set of 11 electrophysiological features, model validation was performed on a different set of 31 electrophysiological features; STAR Methods). The agreement observed between modeling and experimental data is highly non-trivial (Figures 4D and S7). Specifically, while the models are optimized around a set of electrophysiology features, whether they turn out to accurately reflect the experimental data remains questionable, particularly so for differences between two conditions (WG1 vs. WG4) within a particular cell type (human DG GCs). The reason is because the morphologically detailed conductance-based models we generate are non-linear and high dimensional. For any optimization procedure, this is a very demanding scenario since convergence between model and experimental features is not guaranteed. The fact that we show such convergence is non-trivial and speaks to the power and quality of the computational optimization procedure employed. Moreover, the fact that the resulting models exhibit the same type of separation as experiments in an unbiased manner is unique and, once more, speaks to the quality of the parameter optimization procedure and the resulting models. We conclude that the human GC models generated by the computational workflow faithfully reproduce within-cell-type similarities as well as degree-of-pathology differences measured in our experiments.

The development of realistic conductance-based models and the inclusion of 15 distinct ionic conductances shown to express in human GC neurons offers a computational framework to study disease progression changes at a mechanistic level. Pairwise comparison between WG1 vs. WG4 models pointed to three conductances exhibiting the most prominent, WG-related difference: Ca-dependent K channel (BK), Cav2.2, and Kir2.1. Specifically, we found that reducing BK and increasing Cav2.2 and Kir2.1 conductance from their respective WG1 value (percentage change of median conductance from WG1 to WG4: BK, 56% increase; Cav2.2, 28% decrease; Kir2.1: 52% decrease) resulted in electrophysiology properties closely resembling WG4 cases (Figures 4E, left, and S8). To test these model predictions, we also performed snRNA-seq in the resected hippocampal tissue of a subset of our patient cohort (4 out of 7 patients; 2 WG1, 2 WG4) and quantified the expression of genes associated with the three conductances, namely KCNMA1 (BK), CACNA1B (Cav2.2), and KCNJ2 (Kir2.1). We found that the trends (size effect) predicted by the models for the two ionic conductances are supported by the snRNA-seq data (their absolute numbers expressed in unique molecular identifiers [UMIs]). Specifically, we observed upregulation of BK and downregulation of Cav2.2 with disease progression (Figure 4E). Such agreement between conductance level and RNA expression is by no means guaranteed given that snRNA-seq does not necessarily translate to expression of proteins in the membrane. The direction of changes associated with Kir2.1 was inconclusive because of a low number of gene reads.

How do the three identified ion conductances affect changes observed in electrophysiology properties, i.e., the f-I slope and time to first spike? We used the aforementioned single-neuron models and performed a sensitivity analysis by perturbing parameters such as somatic Cav2.2 and Kir2.1 conductances and measuring their impact on the f-I slope and time to first spike (Figure S9). Importantly, the conductance perturbations in this analysis were similar to the ones brought about by the disease progression. Out of the three conductances, we found that only the decrease in somatic Cav2.2 from WG1 to WG4 affected the f-I gain in the same manner as observed experimentally (Figure S9). Moreover, a decrease in dendritic Kir2.1 conductance was the only perturbation that resulted in a reduction of spike latency (Figure S9). It follows that changes in somatic Cav2.2 and dendritic Kir2.1 conductances brought about by the disease best explain the changes observed in the most salient electrophysiology properties, respectively.

Circuit excitability

How are the differences observed at the single-cell level manifested in a network setting? We used the single-neuron models to generate a network mimicking key features of DG circuitry consisting of biophysically realistic and connected excitatory (GCs) and inhibitory (human basket cells [BCs]) neurons (network: 500 GC models, 6 human BCs[19]) (Figure 5A). We tested the role of WG-dependent alterations on network dynamics via two independent manipulations: (1) by altering the network GC composition between WG1 and WG4 GC models while maintaining all other aspects of the network identically (i.e., BC composition, connectivity, synaptic weights, external inputs, etc.) and (2) by doubling the synaptic density between GCs from WG1 to WG4 (Figure 5B). While Poisson-like, external input resulted in asynchronous GC and BC output for an unconnected network (“WG1 no syn”), instantiating recurrent connectivity between WG1 GCs and BCs (“WG1”) resulted in recurring burst activity. We use burst activity as a proxy for hippocampal circuit excitability. During bursting, the WG1 network exhibited an increase of GC firing rate (42 Hz at the peak) accompanied by interneuron firing rate increase (56 Hz at the peak; Figure 5C), with the firing rate between bursts being substantially lower (GCs: approx. 1 Hz; BCs: 10 Hz). Substituting WG1 GC models with WG4 ones while preserving all other aspects of the circuit (“WG4”) resulted in increased frequency of burst occurrence (Figures 5B and 5C). Markedly, increased excitability for the “WG4” network occurred despite WG4 GCs exhibiting decreased spike-frequency gain (Figures 2F and 4C) compared with WG1. This can be attributed to their shorter reaction time (i.e., broadly related to the “time-to-spike” feature), which effectively translates into reduced rheobase. Following our observation of the approximate doubling of spine density from WG1 to WG4 (Figure 3F), we instantiated a 2-fold increase in recurrent connectivity between WG4 GCs in the network (“WG4 ×2”) that resulted in even stronger, sharper, and more frequent burst events (Figures 5B and 5C). Importantly, network excitability is substantially reversed when the three ionic conductances found to be differentially expressed between WG1 and WG4 GCs (BK, Cav2.2, Kir2.1) are substituted in “WG4” GC models with their “WG1”-like values, while all other aspects of the network remained unperturbed (“WG4 alt”). We conclude that GC-specific alterations observed during TLE progression in the human hippocampus can readily lead to increased, recurring circuit excitability congruent with clinical observations of patients with increased HS resulting in more frequent seizures.[5–9] Moreover, combined, disease-related alterations

in BK, Cav2.2, and Kir2.1 conductances predicted via data-driven biophysical modeling and supported by independent snRNA-seq analysis critically influence circuit dynamics dictating the transition from suppressed (WG1) to elevated (WG4) circuit excitability.

DISCUSSION

How cells in the human brain change with disease progression and become hyperexcitable, contributing to TLE seizures, remains unanswered. This is particularly true for neurons in the human hippocampus, a brain region tightly linked to seizure initiation and support. We found that human GCs, a prominent excitatory cell type in the hippocampus that survives disease progression, alter a number of their properties that are significantly affected by TLE and HS progression as witnessed in their genomic signature. How are these changes manifested? Electrophysiologically, the most prominent difference in GCs with disease progression is the decreased f-I gain. Yet, shorter spike latency of WG4 GCs vs. their WG1 counterparts leads to elevated, recurring circuit excitability (despite reduced f-I gain), an observation in line with clinical observations that patients with increased HS typically suffer from an increased number of seizures and an earlier stage of onset.[9,15,16] Our work suggests that alteration of GC and network excitability with disease progression is mainly attributed to changes in three ionic conductances: BK, Cav2.2, and Kir2.1.

In the context of human epilepsies, BK channels have gathered considerable attention, e.g., Du et al.[26] Yet, gain of function of BK exhibited in our patient cohort as well as described in patients of genetic epilepsies has been difficult to explain mechanistically.[27–29] Here, we offer a mechanistic framework relating gain of function in BK channels of human GCs, key regulators of hippocampal excitability,[21] with increased network excitability. Our findings in human GCs also broadly agree with observations in rodents, in which a seizure-induced switch in BK channels results in an excitability increase of cortical and DG neurons.[30,31]

Concurrently, our single-cell perturbation analysis attributed changes in f-I slope and time to first spike in the reduction of the Cav2.2 and Kir2.1 conductances, respectively, during TLE progression. Also referred to as an N-type Ca current, it has been implicated in TLE, with a number of anticonvulsant medications impacting it.[32–35] Notably, our data suggest that to revert disease progression, a gain of function in Cav2.2 is required. Alteration in the expression level of Kir2 channels has also been linked to excitability changes of GCs in TLE.[36,37] While we detected WG-dependent Kir2-conductance differences in our GC models, snRNA-seq revealed that overall expression of these channels is comparatively low (Figure 4B; in agreement with Beck et al.[38]). Notably, correspondence between model-based conductance levels and the transcripts measured by snRNA-seq is welcome, but not guaranteed, as the extent to which RNA expression reflects protein expression in membrane is unclear. Moreover, because conductance-based models accounting for electrophysiology and morphology features are high dimensional and their optimization is non-convex, it cannot be completely excluded that a combination of different conductances can lead to similar cellular phenomenology. Yet, the fact that the models produced in this study in an unsupervised manner and “from first principles” replicate cellular WG-dependent phenomenology as well as give rise to network dynamics that recapitulate functional changes supports the herein presented mechanism as an important candidate.

Using biophysically detailed network simulations, we investigated the role of synaptic connectivity and cellular biophysics in the context of seizure generation. We found that perturbations in ion channel composition as well as network connectivity can bring the network toward a more excitable, highly synchronized state (Figure 5). We found that ion conductance manipulation in a manner that brings the models from WG4 to WG1 (i.e., by adjusting the three conductances from their WG4 to their WG1 level while keeping all other aspects of the network unperturbed) reduced network excitability. Thus, targeting these three conductances and the related ion channels presents itself as a possible drug target for human patients with WG4 epilepsy. At the same time, a spectrum of other cell types has also been implicated in epilepsy pathophysiology in humans as well as in animal models of disease. Our framework of investigation for collecting and reconciling between multimodal cellular data can be used to delineate the changes in and the contribution of other cell types related to human epilepsy pathophysiology.

We also observed significant differences in the morphology and spine density of GCs, with disease progression in cells from severely sclerotic cases exhibiting thicker dendrites and double the spine density.[39] Despite a clear indication that recurrent excitation between GCs impacts network excitability and dynamics, our simulations, in agreement with experiments in rodents,[40] demonstrate that three ionic conductances, if reverted to their WG1 level (i.e., reducing the BK and increasing the Cav2.2 and Kir2.1 conductances by approx. 30%–50%), can substantially reduce network excitability. This is encouraging given that targeting ion channels is an established way of therapeutic intervention compared with bringing about structural changes in cellular morphology. We conclude that such mechanistic understanding of differences brought about with disease progression underlying TLE can improve therapies, e.g., gene therapy approaches targeting specific electrical conductances and/or potentially cellular morphology in a cell-type-specific manner, to reverse the deleterious pathophysiology effects of epilepsy.

Limitations of the study

We used two statistical methods independently, non-parametric Mann-Whitney U testing and random forests, to analyze the electrophysiology and morphology features of single cells and to look at cellular properties associated with disease progression. Both methods independently pointed to the same features separating WG1 from WG4 in terms of electrophysiology and morphology (we also observed the same separation in t-SNE). While this approach offers increased robustness in the analyses and trends observed in this unique human multimodal cellular dataset, the field will benefit from more extensive human snRNA-seq datasets and analysis to fully identify gene expression changes associated with disease progression.

Furthermore, pairwise comparisons between patients having different neuropathological scoring can be prone to patient-specific batch effects. Specifically, neuropathology scoring resulted in all cells from a particular patient receiving the same score (WG1 or WG4), ignoring the fact that different cells may be in a different state during the course of disease development within the same patient. While our study did not address such confounding factors, new methods based on disease trajectory may offer novel insights by assigning the

cells of a given patient to different states along disease progression trajectory (e.g., Saelens et al.[41]).

Conclusion

This work presents a multimodal, single-cell dataset in an effort to understand the diseased brain and how disease progression manifests itself on properties of a major hippocampal cell class, GCs, in human patients with TLE. Our multimodal approach links across scales (from ion channels and single-cell physiology to circuit dynamics and pathophysiology) in the epicenter of the disease, the human hippocampus. These insights shed light on the biophysical underpinnings of the disease while rejecting a few existing hypotheses (e.g., about the key role of Ih in human GCs in TLE). Furthermore, this work has implications beyond TLE and also sheds light on mechanisms related to human seizure disorders in general, as well as disorders related to the same ion channels. Finally, the herein suggested mechanisms will be informative for several disorders implicating GCs as well as other excitatory cells in the human brain.

STAR★METHODS

RESOURCE AVAILABILITY

Lead contact—Further information and requests for resources and reagents should be directed to and will be fulfilled by the lead contact, Costas A. Anastassiou (costas.anastassiou@gmail.com, costasa@alleninstitute.org, costas.anastassiou@cshs.org).

Materials availability—The all-active single-neuron models as well as the single-cell RNA-seq data used in this manuscript are publicly available for download (see key resources table). This study did not generate new unique reagents.

Data and code availability

- This paper analyzes existing, publicly available data. The accession numbers for the datasets are listed in the key resources table.
- Sequencing data is available on Gene Expression Omnibus: GSE216877
- The automated staged optimization workflow is available as a python package, with BluePyOpt being the main procedure for the evolutionary multi-objective optimization. The data analysis, visualization, and the all-active models developed in this work have been deposited in a separate repository. All code is publicly accessible as of the date of publication. DOIs are listed in the key resources table.
- Any additional information required to reanalyze the data reported in this paper is available from the lead contact upon request.

EXPERIMENTAL MODEL AND SUBJECT DETAILS

Human biospecimens and data used for this research was obtained from a study approved by the Swedish Neuroscience Institute's Institutional Review Board and informed consent was

obtained from the participants in this study. Human brain tissue from neurosurgical origin was made available through the generosity of tissue donors, Table S1:

All experiments on human data were performed after receiving the written permission from every patient whose data were used in the study. Excised human brain tissue was collected from the brain within 1–3 min of resection (up to 5 min in rare cases), and transported in chilled, oxygenated ACSF.VII from the hospital to the Allen Institute laboratories within 15–30 min. Tissue was then mounted for slice preparation on the chuck of a Compresstome VF-200 or VF-300 vibrating microtome (Precisionary Instruments) to be sliced perpendicular to pial surface. Each human tissue slice was mounted in the recording chamber and inspected to ensure that the entire hippocampal depth was intact. Regions of the hippocampus were identified visually. Dentate gyrus granule cells along the granule cell layer were targeted for the full dataset. More details on tissue preparation can be found in[42] under section “Electrophysiology overview”. We have not evaluated the influence of sex on our results, all data were pooled together.

METHOD DETAILS

Single nucleus RNA sequencing analysis—Intact nuclei from the hippocampus of four human tissue donors — H16.06.008 (WG1), H17.06.015 (WG1), H16.06.009 (WG4) and H16.06.010 (WG4) — were collected and processed for sequencing using 10x Genomics as follows. To generate single nuclei, flash frozen hippocampal samples were Dounce homogenized, stained with mouse anti-NeuN antibody (Millipore, FCMAB317PE), and NeuN+ (~70%) and NeuN− (~30%) nuclei were collected using fluorescence-activated cell sorting (FACS). Sorted nuclei suspensions were concentrated to ~1000 nuclei/μl and loaded onto a 10x Genomics version 3 single-cell RNA-sequencing chip with a targeted capture of ~8000 nuclei per specimen. Nuclei (n = 29,212) were sequenced at a median read depth of 83,474 ± 24,111 reads/nucleus (median ±standard deviation). Median gene detection was 5295 ± 240 genes/nucleus and the median number of UMIs/nucleus was 16,088 ± 1790. For more information on RNA-seq technology applied in human brain tissue, see.[43,44]

RNA-seq data was curated to remove nuclei with less than 1′000 genes detected, leaving 27,242 nuclei remaining. Nuclei were then assigned to broad classes (GCs, other excitatory, inhibitory, and non-neuronal) via supervised clustering (k = 4), using the 100 most selective genes for each class. GC genes were defined as genes with the most significant differential expression between “DG” and “HiF” (Hippocampal Formation) in the “Differential Search” in the Allen Human Brain Atlas (http://human.brain-map.org/ [25]). Similarly, markers for the other classes were selected using the RNA-seq Data Navigator: Human—a part of the Allen Cell Types Database (http://celltypes.brain-map.org [44]) — by running “Find Marker Genes” for “Cell Category” against all other cells. This identified genes specific for each class based on single nucleus RNA-seq in human middle temporal gyrus. The RNA-seq data was normalized by taking the unique molecular identifier (UMI) count for each cell, calculating counts per million (CPM), transforming the data to zero mean and unit variance and then converting it to logarithmic space: EXPR_norm = log2 (CPM(UMI)+1). We then performed supervised *k*-means clustering with $k = 4$ on all normalized data (4158 genes)

for nuclei using only these differential genes to identify cells most likely corresponding to each cell class. 12′011, 6′386, 5′302, and 3′543 nuclei were found corresponding to GCs, other excitatory, inhibitory, and non-neuronal cells, respectively. Expression of selected ion channels across broad classes is shown in Figure 4B. For dimensionality reduction we used the Seurat method[45] and performed principal component analysis using the first 30 principal components. For the visualizations we used the first two principal components.

Integration of the normalized sn RNA-seq data was performed using scvi-tools v0.14 (https://scvi-tools.org/) and scanpy v1.9 (https://scvi-tools.org/). To compensate for batch-effects associated with samples from different patients, we used the patient ID for all cells from the same patient as a batch-parameter. The low-dimensional embedding is computed based on a variational auto-encoder trained on gene expression data from GCs using scvi-tools. We used the following variational auto-encoder neural network architecture: 100 (input layer), 10 (internal layer) and 100 (output layer). The network was trained using the stochastic gradient descend algorithm. We used standard parameters provided by scvi-tools v0.14. In the final stage, we applied UMAP on the internal network representation of the data provided by the auto-encoder. For the final data visualization, we used 2 dimensions from UMAP algorithm (UMAP1, UMAP2). For pairwise comparisons between WG1 and WG4 granule cells we used Wilcoxon signed rank test implemented in scanpy.

For the differential gene expression analysis, we used the ‘rank_genes_groups’ function from scanpy together with the Wilcoxon rank-sum test. All computations were performed on normalized data. After pairwise testing, genes were ranked according to Z score and the top 20 genes were reported.

Slice electrophysiology—For electrophysiological recordings, human brain slices were mounted in a custom designed chamber and held in place with a slice anchor (Warner Instruments). The slice was bathed in ACSF at 34 ± 1°C (warmed by an npi hpt-2 flow-through heater and thermafoil, controlled by an npi TC-20) at a rate of 2 mL per minute (Gilson Minipuls 3 pump). As a target temperature, 34°C was chosen to approximate physiological conditions, but with a safety buffer so as to not exceed 37°C. Bath temperature was continuously monitored. ACSF oxygenation was maintained by bubbling 95% O2, 5% CO2 gas in the specimen reservoir as well as delivering across the surface of the incubation bath via the custom designed specimen chamber. Solution oxygen levels, temperature and flow rate were monitored; values were measured, documented, and calibrated weekly to verify system quality.

Thick walled borosilicate glass (Sutter BF150-86-10) electrodes were manufactured (Sutter P1000 electrode puller) with a resistance of 3–7 MΩ. Prior to recording, electrodes were filled with 20 μL of internal solution SOP consisting of potassium gluconate, HEPES and other components[42] with biocytin, which was thawed fresh every day and kept on ice. The pipette was mounted on a Multiclamp 700B amplifier headstage (Molecular Devices) fixed to a micromanipulator (PatchStar, Scientifica).

Electrophysiology signals were recorded using an ITC-18 Data Acquisition Interface (HEKA). Commands were generated, signals processed, and amplifier metadata was

acquired using a custom acquisition software program, written in Igor Pro (Wavemetrics). Data were filtered (Bessel) at 10 kHz and digitized at 50 kHz. Data were reported uncorrected for the measured −14 mV liquid junction potential between the electrode and bath solutions.

Upon break-in and formation of a stable seal (typically within the first minute and not more than 3 min after break-in), the resting membrane potential of the neuron was recorded. All recordings were bridge balanced and systematically checked for access resistance matching the quality control criteria described in[46] under section “Electrophysiology overview”.

Electrophysiological feature analysis—For the electrophysiological feature analysis we used the AllenSDK library (https://allensdk.readthedocs.io/en/latest/) to extract passive and spiking features from electrophysiological recordings of single neurons and biophysical models, Table S2. The same set of features was used for Figure 4 and all other electrophysiology analyses.

To perform the dimensionality reduction of the electrophysiological data we first normalized (zero mean and unit variance) the features in our analysis (Table S2). Next, we applied the tSNE with the perplexity parameter equal to 30. We also performed additional runs of tSNE algorithm on the data with different perplexity values to ensure the stability of the results. Finally, we used *k*-means clustering with $k = 2$ to find the boundaries between WG1 and WG4 cells and visualized the projection on the tSNE plot in Figure 2B (broken line).

Morphology reconstruction and feature extraction—Morphological reconstructions were generated using previously described methods[42] under section “Morphology and Histology Overview”. Briefly, biocytin-filled neurons were stained via diaminobenzidine reaction and imaged at 63x magnification on a Zeiss Axio Imager 2. Individual cells were digitally reconstructed with custom-written software (Vaa3D and Mozak) to create accurate, whole-neuron representations saved in the SWC format (Figure S10). A feature extraction suite was adopted and customized enabling the analysis of dendritic and somatic reconstructions and extraction of a number of features related to branching pattern, size, density, soma position, etc. resulting in 49 morphology features (Table S4).

Dendritic spine densities were assessed using Neurolucida 360 (v2017.01.1) and Imaris (v9.3). Initial and terminal 100 μm sections of the dendritic region outside the granule cell layer were visualized for manual spine density estimation along 10 μm-long segments per dendritic branch.

To perform the dimensionality reduction of the morphological features we first normalized the morphological features (zero mean, unit variance). Then, we applied tSNE to project the data in 2 dimensions. Every cell in Figure 3 is colored according to its WG-group (WG1: blue; WG4: red). Finally, we performed *k*-means clustering on all 49 normalized morphology features (Table S4) and show the 2 dimensional projection in Figure 3B (broken line).

QUANTIFICATION AND STATISTICAL ANALYSIS

Data analysis—We used the standard scientific Python libraries for analyzing the electrophysiological and morphological data: Mann-Whitney U-testing (mannwhitneyu with p value = 0.05 with Bonferroni correction, statistics library), random forest classification (RandomForestClassifier with 200 decision trees, gini impurity, min_samples per leaf = 1, min samples per split = 2, out of bag score for classification, scikit-learn) and regression analysis (least squares method, numpy library). All corresponding p values and numbers of samples are present in relevant figure captions. All univariate statistical tests were performed on Figures 2, 3, 4, 5, S2, S3, S5, S7, and S8 with Bonferoni corrections for multiple comparisons. We used non-parametric methods, such as Mann-Whithney U-testing for all relevant pairwise comparisons. In Figure 2, we compared electrophysiological features; in Figure 3, we compared morphological features and average spine density per neuron; in Figure 4, we compared the estimated conductances from the computational models and UMI counts in snRNA-seq data; in Figure 5, we compared the properties of burst events in biological neural network; in Figure S2, we compared the numbers of cells; in Figure S3, we compared the UMI counts; in Figure S5, we compared the morphological and electrophysiological properties; in Figure S7, we compared the electrophysiological properties; in Figure S8, we compared the computational model conductances. The mean of the distribution was used to compare the effect size and the standard deviation as a measure of the spread (shown in error bars). We used pairwise comparisons and analyzed the classifier weights (random forest) for hypothesis testing. All comparisons were performed using scipy Python package version 1.9.3 For the random forest classifier, we tested whether increasing the tree number in the forest improves the classification score and found it was not the case. For dimensionality reduction, we used tSNE as implemented in the sklearn.manifold package and used perplexity equal to 30. Notably, we also evaluated tSNE for a number of perplexity values (10, 20, 30, 40, 50) to ensure the stability of the results and found that the main outcomes of analysis remained broadly unchanged.

Electrophysiology feature extraction and single-cell model setup—From whole-cell patch-clamping experiments, electrophysiological responses to a battery of standardized current stimuli (1 s-long dc current injections of increasing amplitude) were analyzed resulting in a set of subthreshold and spiking features for each experiment (Table S2). Electrophysiology features such as spike timing, amplitude, width, etc. were obtained for each experiment. For a subset of features, regression was used to assess how a particular electrophysiology feature changes with increasing intracellular stimulation amplitude. In total, 30 electrophysiology features were extracted from our *in vitro* experiments (Table S2) and analyzed with a number of statistical techniques for WG-dependent differences. Details on the implementation of the feature extraction analysis and relevant code is publicly available through.[47]

The model optimization procedure for generating biophysically realistic single-neuron models is feature-based and attempts to set the somatic, axon initial segment, and dendritic properties in such manner to capture features of intracellular somatic responses for a number of standardized current stimulation waveforms. For model generation, electrophysiology features were extracted using a feature extraction library (eFEL) developed in.[48]

Specifically, 11 electrophysiology features were extracted for each experiment (Figure S4) and their mean and standard deviation (std) was computed for a particular stimulation waveform. If more than one sweep of the same stimulation waveform exists (majority of the experiments), then the std of that particular waveform was used. If only a single sweep of the experiment exists, a default value of 10% was used for the std.

The compartments of human granule and basket cells were separated into three zones: the axon initial segment (AIS), the soma and dendrites. In our models, the AIS was represented by one fixed-length section with a total length of 30 μm and 1 μm diameter.

In all models, passive and active properties were optimized using the same fitting procedure. For passive properties, one value for the specific capacitance (cm), passive conductance (g_pas), passive reversal potential (e_pas), and cytoplasmic resistivity (Ra) was uniformly set across all compartments. Notably, the values of these parameters were part of the genetic optimization procedure (see below). Active channel mechanisms were spatially uniformly distributed in the AIS, soma, and dendrites with every zone receiving a separate set of channels (Tables S5 and S6).

We used the model generation workflow to create the biophysically detailed models of excitatory granule cells from human hippocampus as well as the inhibitory basket cells from human medial temporal gyrus (neocortex). The latter are used in Figure 5. For the human inhibitory basked cells, the morphological and electrophysiological data originate from[46] (specimen IDs: 529,807,751, 541,536,216; Table S6).

The final set of excitatory and inhibitory models are available on: https://github.com/anastassiou-team/human-epilepsy-project. The dentate gyrus circuit model is available under: https://github.com/anastassiou-team/human-epilepsy-project/tree/master/Fig_5/network_simulations. The Github repo has been added to a Zenodo repository: https://zenodo.org/badge/latestdoi/256053700.

Parameter optimization and single-cell generation workflow—For the single-cell model optimization and generation, the BluePyOpt framework was adopted (https://github.com/AllenInstitute/All-active-Workflow, https://github.com/AllenInstitute/All-active-Manuscript, https://github.com/AllenInstitute/epilepsy_human_dg_public) [48] which utilizes multi-objective optimization relying on an evolutionary optimization algorithm. Every cell used for the optimization had two data modalities present: a unique reconstructed morphology as well as a set of ephys features (see previous sections). It follows that the morphology of each model was unique and not identical with one exception: in Figure 4E, 10 models per cell were produced in order to pursue pairwise conductance comparisons (see also next section). For the rest, the rule “one-model-per-cell each with a unique morphology and set of ephys properties” applies.

After performing the simulations of the biophysical models, the time traces of the model output was analyzed. For every time trace, a standard set of electrophysiological features was analyzed and extracted (Table S2). In order to develop and optimize the single-cell models, a smaller set of electrophysiology features needed to be considered as the

computational cost and complexity strongly depends on the number of objectives used for the multi-objective, genetic optimization. We decided to use 11 electrophysiological features for the multi-objective optimization (Figure S6). For every feature, an absolute standard score was calculated $Z_i = |f_i - \mu_i|/\sigma_i$ with the current feature value (f_i) measured from the output traces of the models and μ_i, σ_i being the experimentally measured mean and standard deviation, respectively.[48]

The development of every biophysically detailed single-cell model involved a 3-stage optimization workflow that iteratively focused on a set of conductances. In the first stage, passive model properties like membrane resistance and capacitance were set by fitting subthrehold responses and subthreshold features such as *voltage_sag*, *voltage_base* and *voltage_after_stim* (Table S2). In the second stage, 15 active ionic conductances were included while keeping the membrane capacitance and passive reversal potential fixed. Notably, the initial parameter ranges for all GC models (both for passive and active ion channels) were chosen irrespective of WG (Table S5) and optimized for 100 generations. In this stage, ten spiking traces were used for model training along with subthreshold responses. In the final stage, the best model from the previous stage was chosen, its parameter range extended by two-fold for all conductances and optimization was re-initialized for at least 50 generations. As part of the BluePyOpt framework, multiple models were generated for every cell with the best individual considered after ranking and measuring their performance performance on the training set (best model: the smallest sum of objective values). The best model for each experiment was used in the pool of models selected for the network simulations (Figure 5). Concurrently, for every cell, the 10 best models ("hall of fame" models according to[48]) were selected and used for pairwise conductance comparisons between WG1 and WG4 (Figure S8).

For the multi-objective evolutionary algorithm used to generate the single-cell models, a population size of typically 320 individual models per cell on 320 cores of a BlueGene/P or Cori Haswell (Cray XC40) supercomputer was used. Generation of a single, biophysically detailed, single-neuron model required approximately 200′000 core-hours of computational time on the aforementioned architectures.

Biophysical model selection—Every cell has been optimized with 10 electrophysiological spiking traces as well as a number subthreshold voltage traces (range: −90 to −60 mV). The cellular morphology was reconstructed in 3d in a supervised manner from experiments where electrophysiological recordings were performed. In a subset of experiments, biocytin staining did not allow for the cellular morphology reconstruction resulting in the difference between the number of experiments with electrophysiology vs. reconstructed morphologies (cells with ephys vs. morphology reconstructions; for WG1: 61 vs. 52; for WG4: 51 vs. 50).

The pool of cells used to generate models was 2 cells from case H16.06.008 (WG1), 6 cells from H16.06.013 (WG4), 11 cells from H17.06.012.21 (WG4), 11 cells from H17.06.014 (WG1), and 12 cells from H17.06.015 (WG1). The best 12 models (model quality assessed by the distance between experiments and model features) were chosen for Wyler grade 1 and 4 comparisons stratified by the patients. For the pairwise comparisons of model

conductances (Figures 4 and S8), we used a slightly different approach. Specifically, we decided to produce multiple models per cell, as the multi-objective optimization framework allows it. Then, we chose the 10 best models per cell coming out of the multi-objective optimization procedure (sometimes referred to as “hall-of-fame” models). Since each Wyler grade was represented by 12 cells, each Wyler grade group comprised of (12 cells) × (10 models per cell) = 120 models. The statistical comparison was then performed in a pairwise fashion across active conductance parameters for all models of each group.

Hippocampal network model setup—A bio-plausible DG network model was constructed consisting of 506 single-cell models with the details of the network relying on.[19] Briefly, GC and BC cells in our network were positioned via a topographic approach with somata of the models positioned in 3D space along a ring with a radius of 1500 μm for GCs and 750 μm for BCs. The ring was opened to form the arch roughly corresponding to the physical extent of human DG (Figure 5A).

Synaptic connectivity in the network depends on the location of a neuron along the ring (characterized by the arch-angle). The overall neural network structure was adapted from.[19] We have modified the number of connections per synapse to make it more realistic and in agreement to.[49] The following connectivity structure was chosen to represent the DG circuit with periodic boundary conditions (compensating for border artifacts). Every GC formed 50 connections with its 100 closest GCs along the ring with the exact connectivity between the postsynaptic target pool chosen randomly. Every GC also projected to 3 of its closest BCs along the ring. Recurrent GC-GC connections formed 2 to 5 synapses with the exact number chosen randomly. The location of GC synapses was chosen along dendrites within 150 μm from the soma. All excitatory connections of GCs corresponded to AMPA synapse kinetics.[19]

Every BC created 100 out of 140 possible connections with its topographically closest GCs with synapses located on the soma of GCs. Recurrent BC connectivity was also implemented so that every BC is connected to its two closest neighbors with the exact location of inhibitory synapses chosen randomly within 150 μm from the BC soma. All inhibitory connections correspond to GABA-A synapse kinetics.[19] Synaptic kinetics were approximated using biexponential synapse models (‘exp2syn′ in[50]) involving two time constants (τ_1 and τ_2) as well as the reversal potential (V_{rev}). The values used for these parameters are the following (adopted from[19]):

To activate the network, GCs and BCs received background synaptic input along their dendrites. GCs received 5 external connections per cell with 5–15 synapses each – the exact number of synapses was chosen randomly from a homogeneous distribution. BCs received the same amount of background synaptic input. Every background connection was activated by a Poisson process (rate: 3 Hz) emulating perforant path input. Background synaptic input corresponded to AMPA synapse kinetics both for GCs and BCs.[19]

All network simulations were setup and performed using inhouse developed software based on.[51] The versions of the DG network presented in Figure 5 is publicly available through https://github.com/AllenInstitute/epilepsy_human_dg.

Supplementary Material

Refer to Web version on PubMed Central for supplementary material.

ACKNOWLEDGMENTS

We wish to thank Allen Institute founder Paul G. Allen for his vision, encouragement, and support. We thank Brandon Blanchard and Kael Dai for assisting with illustrations; Soo Yeun Lee, Tom Chartrand, Yina Wei, and Bosiljka Tasic for discussions; and Lynne Becker for transitional project management support. We thank the Allen Institute Tissue Procurement team, especially Nick Dee, Julie Nyhus, Rusty Nikovich, and Facilities team members, for supporting human surgical tissue acquisition and transport. We are grateful to Caryl Tongco and Jae-Guen Yoon at the Swedish Neuroscience Institute/Swedish Medical Center for coordinating patient consent, patient metadata, and tissue collections. We thank Dr. Carter Gerard for discussions and consultation early in the project, Dr. Ivan Soltesz for discussions and suggested analyses, and Drs. Rostad and Driscoll for providing deidentified patient tissue pathology reports. We thank the Cedars-Sinai Medical Center and the Allen Institute for Brain Science for the financial support. C.A.A. acknowledges NIH grant RO1 NS120300*01. This research used resources of the National Energy Research Scientific Computing Center, a DOE Office of Science User Facility supported by the Office of Science of the US Department of Energy under contract no. DE-AC02- 05CH11231.

REFERENCES

1. Kwan P, and Sander JW (2004). The natural history of epilepsy: an epidemiological view. J. Neurol. Neurosurg. Psychiatry 75, 1376–1381. [PubMed: 15377680]
2. Fuerst D, Shah J, Shah A, and Watson C (2003). Hippocampal sclerosis is a progressive disorder: a longitudinal volumetric MRI study. Ann. Neurol. 53, 413–416. 10.1002/ana.10509. [PubMed: 12601713]
3. Wiebe S, Blume WT, Girvin JP, and Eliasziw M; Effectiveness and Efficiency of Surgery for Temporal Lobe Epilepsy Study Group (2001). A randomized, controlled trial of surgery for temporal-lobe epilepsy. N. Engl. J. Med. 345, 311–318. 10.1056/NEJM200108023450501. [PubMed: 11484687]
4. Spencer S, and Huh L (2008). Outcomes of epilepsy surgery in adults and children. Lancet Neurol. 7, 525–537. 10.1016/S1474-4422(08)70109-1. [PubMed: 18485316]
5. Vossler DG, Kraemer DL, Knowlton RC, Kjos BO, Rostad SW, Wyler AR, Haltiner AM, Hasegawa H, and Wilkus RJ (1998). Temporal ictal electroencephalographic frequency correlates with hippocampal atrophy and sclerosis. Ann. Neurol. 43, 756–762. 10.1002/ana.410430610. [PubMed: 9629845]
6. Kälviäinen R, Salmenperä T, Partanen K, Vainio P, Riekkinen P, and Pitkänen A (1998). Recurrent seizures may cause hippocambal damage in temporal lobe epilepsy. Neurology 50, 1377–1382. [PubMed: 9595990]
7. Salmenperä T, Kälviäinen R, Partanen K, and Pitkänen A (2001). Hippocampal and amygdaloid damage in partial epilepsy: a cross-sectional MRI study of 241 patients. Epilepsy Res. 46, 69–82. 10.1016/S0920-1211(01)00258-3. [PubMed: 11395291]
8. Vossler DG, Kraemer DL, Haltiner AM, Rostad SW, Kjos BO, Davis BJ, Morgan JD, and Caylor LM (2004). Intracranial EEG in temporal lobe epilepsy: location of seizure onset relates to degree of hippocampal pathology. Epilepsia 45, 497–503. 10.1111/j.0013-9580.2004.47103.x. [PubMed: 15101831]
9. Kälviäinen R, and Salmenperä T (2002). Do recurrent seizures cause neuronal damage? A series of studies with MRI volumetry in adults with partial epilepsy. In Progress in Brain Research Do Seizures Damage the Brain (Elsevier), pp. 279–295. 10.1016/S0079-6123(02)35026-X.
10. Dunleavy M, Schindler CK, Shinoda S, Crilly S, and Henshall DC (2014). Neurogenic function in rats with unilateral hippocampal sclerosis that experienced early-life status epilepticus. Int. J. Physiol. Pathophysiol. Pharmacol. 6, 199–208. [PubMed: 25755841]
11. Spencer SS, McCarthy G, and Spencer DD (1993). Diagnosis of medial temporal lobe seizure onset: relative specificity and sensitivity of quantitative MRI. Neurology 43, 2117–2124. [PubMed: 8413976]

12. Jokeit H, Ebner A, Arnold S, Schüller M, Antke C, Huang Y, Steinmetz H, Seitz RJ, and Witte OW (1999). Bilateral reductions of hippocampal volume, glucose metabolism, and Wada hemispheric memory performance are related to the duration of mesial temporal lobe epilepsy. J. Neurol. 246, 926–933. 10.1007/s004150050484. [PubMed: 10552240]

13. Seeck M, Lazeyras F, Murphy K, Naimi A, Pizzolatto GP, de Tribolet N, Delavelle J, Villemure J-G, and Landis T (1999). Psychosocial functioning in chronic epilepsy: relation to hippocampal volume and histopathological findings. Epileptic Disord. 1, 179–185. [PubMed: 10937151]

14. Fuerst D, Shah J, Kupsky WJ, Johnson R, Shah A, Hayman–Abello B, Ergh T, Poore Q, Canady A, and Watson C (2001). Volumetric MRI, pathological, and neuropsychological progression in hippocampal sclerosis. Neurology 57, 184–188. [PubMed: 11468300]

15. Trenerry MR, Jack CR, Sharbrough FW, Cascino GD, Hirschorn KA, Marsh WR, Kelly PJ, and Meyer FB (1993). Quantitative MRI hippocampal volumes: association with onset and duration of epilepsy, and febrile convulsions in temporal lobectomy patients. Epilepsy Res. 15, 247–252. 10.1016/0920-1211(93)90062-C. [PubMed: 8223421]

16. Keller SS, Wieshmann UC, Mackay CE, Denby CE, Webb J, and Roberts N (2002). Voxel based morphometry of grey matter abnormalities in patients with medically intractable temporal lobe epilepsy: effects of side of seizure onset and epilepsy duration. J. Neurol. Neurosurg. Psychiatry 73, 648–655. 10.1136/jnnp.73.6.648. [PubMed: 12438464]

17. Wyler AR, Curtis Dohan F, Schweitzer JB, and Berry AD (1992). A grading system for mesial temporal pathology (hippocampal sclerosis) from anterior temporal lobectomy. J. Epilepsy 5, 220–225. 10.1016/S0896-6974(05)80120-3.

18. Kalmbach BE, Buchin A, Long B, Close J, Nandi A, Miller JA, Bakken TE, Hodge RD, Chong P, de Frates R, et al. (2018). H-channels contribute to divergent intrinsic membrane properties of supragranular pyramidal neurons in human versus mouse cerebral cortex. Neuron 100, 1194–1208.e5. 10.1016/j.neuron.2018.10.012. [PubMed: 30392798]

19. Santhakumar V, Aradi I, and Soltesz I (2005). Role of mossy fiber sprouting and mossy cell loss in hyperexcitability: a network model of the dentate gyrus incorporating cell types and axonal topography. J. Neurophysiol. 93, 437–453. 10.1152/jn.00777.2004. [PubMed: 15342722]

20. Morgan RJ, and Soltesz I (2008). Nonrandom connectivity of the epileptic dentate gyrus predicts a major role for neuronal hubs in seizures. Proc. Natl. Acad. Sci. USA 105, 6179–6184. 10.1073/pnas.0801372105. [PubMed: 18375756]

21. Goldberg EM, and Coulter DA (2013). Mechanisms of epileptogenesis: a convergence on neural circuit dysfunction. Nat. Rev. Neurosci. 14, 337–349. 10.1038/nrn3482. [PubMed: 23595016]

22. van der Maaten L, and Hinton G (2008). Visualizing Data using t-SNE. J. Mach. Learn. Res. 9, 2579–2605.

23. Koch C (2004). Biophysics of Computation: Information Processing in Single Neurons (Oxford University Press).

24. Beining M, Mongiat LA, Schwarzacher SW, Cuntz H, and Jedlicka P (2017). T2N as a new tool for robust electrophysiological modeling demonstrated for mature and adult-born dentate granule cells. Elife 6, e26517. 10.7554/eLife.26517. [PubMed: 29165247]

25. Hawrylycz MJ, Lein ES, Guillozet-Bongaarts AL, Shen EH, Ng L, Miller JA, van de Lagemaat LN, Smith KA, Ebbert A, Riley ZL, et al. (2012). An anatomically comprehensive atlas of the adult human brain transcriptome. Nature 489, 391–399. 10.1038/nature11405. [PubMed: 22996553]

26. Du W, Bautista JF, Yang H, Diez-Sampedro A, You S-A, Wang L, Kotagal P, Lüders HO, Shi J, Cui J, et al. (2005). Calcium-sensitive potassium channelopathy in human epilepsy and paroxysmal movement disorder. Nat. Genet. 37, 733–738. 10.1038/ng1585. [PubMed: 15937479]

27. N'Gouemo P (2011). Targeting BK (big potassium) channels in epilepsy. Expert Opin. Ther. Targets 15, 1283–1295. 10.1517/14728222.2011.620607. [PubMed: 21923633]

28. Leo A, Citraro R, Constanti A, De Sarro G, and Russo E (2015). Are big potassium-type Ca2+-activated potassium channels a viable target for the treatment of epilepsy? Expert Opin. Ther. Targets 19, 911–926. 10.1517/14728222.2015.1026258. [PubMed: 25840593]

29. Köhling R, and Wolfart J (2016). Potassium channels in epilepsy. Cold Spring Harb. Perspect. Med. 6, a022871. 10.1101/cshperspect.a022871. [PubMed: 27141079]

30. Shruti S, Clem RL, and Barth AL (2008). A seizure-induced gain-of-function in BK channels is associated with elevated firing activity in neocortical pyramidal neurons. Neurobiol. Dis. 30, 323–330. 10.1016/j.nbd.2008.02.002. [PubMed: 18387812]

31. Whitmire LE, Ling L, Bugay V, Carver CM, Timilsina S, Chuang H-H, Jaffe DB, Shapiro MS, Cavazos JE, and Brenner R (2017). Downregulation of KCNMB4 expression and changes in BK channel subtype in hippocampal granule neurons following seizure activity. PLoS One 12, e0188064. 10.1371/journal.pone.0188064. [PubMed: 29145442]

32. Stefani A, Spadoni F, and Bernardi G (1997). Differential inhibition by riluzole, lamotrigine, and phenytoin of sodium and calcium currents in cortical neurons: implications for neuroprotective strategies. Exp. Neurol. 147, 115–122. 10.1006/exnr.1997.6554. [PubMed: 9294408]

33. Stefani A, Spadoni F, and Bernardi G (1998). Gabapentin inhibits calcium currents in isolated rat brain neurons. Neuropharmacology 37, 83–91. 10.1016/S0028-3908(97)00189-5. [PubMed: 9680261]

34. Schumacher TB, Beck H, Steinhäuser C, Schramm J, and Elger CE (1998). Effects of phenytoin, carbamazepine, and gabapentin on calcium channels in hippocampal granule cells from patients with temporal lobe epilepsy. Epilepsia 39, 355–363. 10.1111/j.1528-1157.1998.tb01387.x. [PubMed: 9578025]

35. Remy S, and Beck H (2006). Molecular and cellular mechanisms of pharmacoresistance in epilepsy. Brain 129, 18–35. 10.1093/brain/awh682. [PubMed: 16317026]

36. Stegen M, Young CC, Haas CA, Zentner J, and Wolfart J (2009). Increased leak conductance in dentate gyrus granule cells of temporal lobe epilepsy patients with Ammon's horn sclerosis. Epilepsia 50, 646–653. 10.1111/j.1528-1167.2009.02025.x. [PubMed: 19292756]

37. Stegen M, Kirchheim F, Hanuschkin A, Staszewski O, Veh RW, and Wolfart J (2012). Adaptive intrinsic plasticity in human dentate gyrus granule cells during temporal lobe epilepsy. Cereb. Cortex 22, 2087–2101. 10.1093/cercor/bhr294. [PubMed: 22038909]

38. Beck H, Clusmann H, Kral T, Schramm J, Heinemann U, and Elger CE (1997). Potassium currents in acutely isolated human hippocampal dentate granule cells. J. Physiol. 498, 73–85. [PubMed: 9023769]

39. Isokawa M (2000). Remodeling dendritic spines of dentate granule cells in temporal lobe epilepsy patients and the rat pilocarpine model. Epilepsia 41, S14–S17. 10.1111/j.1528-1157.2000.tb01550.x. [PubMed: 10999513]

40. Heng K, Haney MM, and Buckmaster PS (2013). High-dose rapamycin blocks mossy fiber sprouting but not seizures in a mouse model of temporal lobe epilepsy. Epilepsia 54, 1535–1541. 10.1111/epi.12246. [PubMed: 23848506]

41. Saelens W, Cannoodt R, Todorov H, and Saeys Y (2019). A comparison of single-cell trajectory inference methods. Nat. Biotechnol. 37, 547–554. 10.1038/s41587-019-0071-9. [PubMed: 30936559]

42. Documentation - allen cell types Database. http://help.brain-map.org/display/celltypes/Documentation?preview=/8323525/10813530/CellTypes_Morph_Overview.pdf.

43. RNA-seq data :: allen brain atlas: cell types. http://celltypes.brain-map.org/rnaseq.

44. Hodge RD, Bakken TE, Miller JA, Smith KA, Barkan ER, Gray-buck LT, Close JL, Long B, Johansen N, Penn O, et al. (2019). Conserved cell types with divergent features in human versus mouse cortex. Nature 573, 61–68. 10.1038/s41586-019-1506-7. [PubMed: 31435019]

45. Satija R, Farrell JA, Gennert D, Schier AF, and Regev A (2015). Spatial reconstruction of single-cell gene expression data. Nat. Biotechnol. 33, 495–502. 10.1038/nbt.3192. [PubMed: 25867923]

46. . Cell features :: allen brain atlas: cell types. http://celltypes.brain-map.org/data.

47. allensdk.ephys package — Allen SDK dev documentation. http://alleninstitute.github.io/AllenSDK/allensdk.ephys.html.

48. Van Geit W, Gevaert M, Chindemi G, Rössert C, Courcol J-D, Muller EB, Schürmann F, Segev I, and Markram H (2016). BluePyOpt: leveraging open source software and cloud infrastructure to optimise model parameters in neuroscience. Front. Neuroinform. 10, 17. 10.3389/fninf.2016.00017. [PubMed: 27375471]

49. Markram H, Muller E, Ramaswamy S, Reimann MW, Abdellah M, Sanchez CA, Ailamaki A, Alonso-Nanclares L, Antille N, Arsever S, et al. (2015). Reconstruction and simulation of neocortical microcircuitry. Cell 163, 456–492. 10.1016/j.cell.2015.09.029. [PubMed: 26451489]

50. Hines ML, and Carnevale NT (1997). The NEURON simulation environment. Neural Comput. 9, 1179–1209. [PubMed: 9248061]

51. Gratiy SL, Billeh YN, Dai K, Mitelut C, Feng D, Gouwens NW, Cain N, Koch C, Anastassiou CA, and Arkhipov A (2018). BioNet: a Python interface to NEURON for modeling large-scale networks. PLoS One 13, e0201630. 10.1371/journal.pone.0201630. [PubMed: 30071069]

Highlights

- Transcriptomics in human granule cells separate early vs. late disease state
- Phenotypic changes in human granule cells occur across modalities
- Changes in granule cell excitability are linked to three ionic conductances

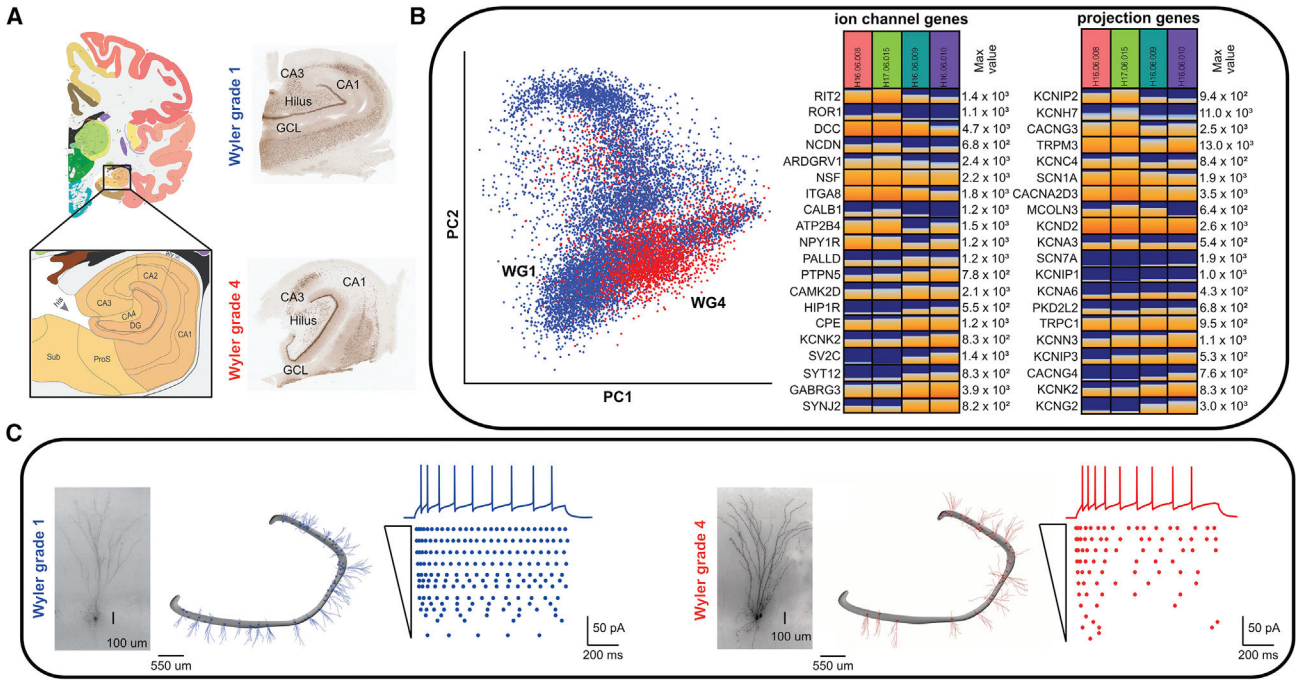

Figure 1. Human data collection from patients with drug-resistant temporal lobe epilepsy

(A) Human dentate gyrus (DG), cornu ammonis (CA) 1–4, and pro-subiculum (ProS) and subiculum (Sub) areas typically resected during temporal lobectomy.

(B) Single-cell gene expression data of 230 ion-channel-coding and 1,600 projection-coding genes specific for human granule cells separate cells with respect to disease state. Left: principal-component analysis of 1,600 projection genes for nuclei with the expression profiles mapped to human DG granule cells. Only the first 2 components are shown. Right: expression level of ion channel and projection genes for different patients (n = 2 for Wyler grade 1, n = 2 for Wyler grade 4). Rows correspond to genes and columns to patients. Expression levels are shown in counts per million (CPM) base pairs. Colors correspond to the minimal and maximal value of gene expression of the particular cell type. Warmer colors correspond to high levels of expression, and colder ones correspond to low levels of expression. The max value of gene expression is shown on the right for every gene.

(C) Human hippocampal slices retrieved from surgical specimens (DG granule cell [GC] layer designated by neuronal nuclei stain). Hippocampal sclerosis (HS), as assessed by Wyler grade, is associated with cell loss in hippocampal subfields such as CA1 (e.g., compare cellular density in area CA1 for WG1 versus WG4 in A). Locations along the human DG where whole-cell patch clamping and morphological reconstructions were gathered across patients. Somatic trace (top) and raster (bottom; lines: experiment trials from the same cell) from whole-cell patch-clamp experiments involving intracellular somatic current dc injection of increasing magnitude in DG GCs from a WG1 (blue) and a WG4 (red) patient case.

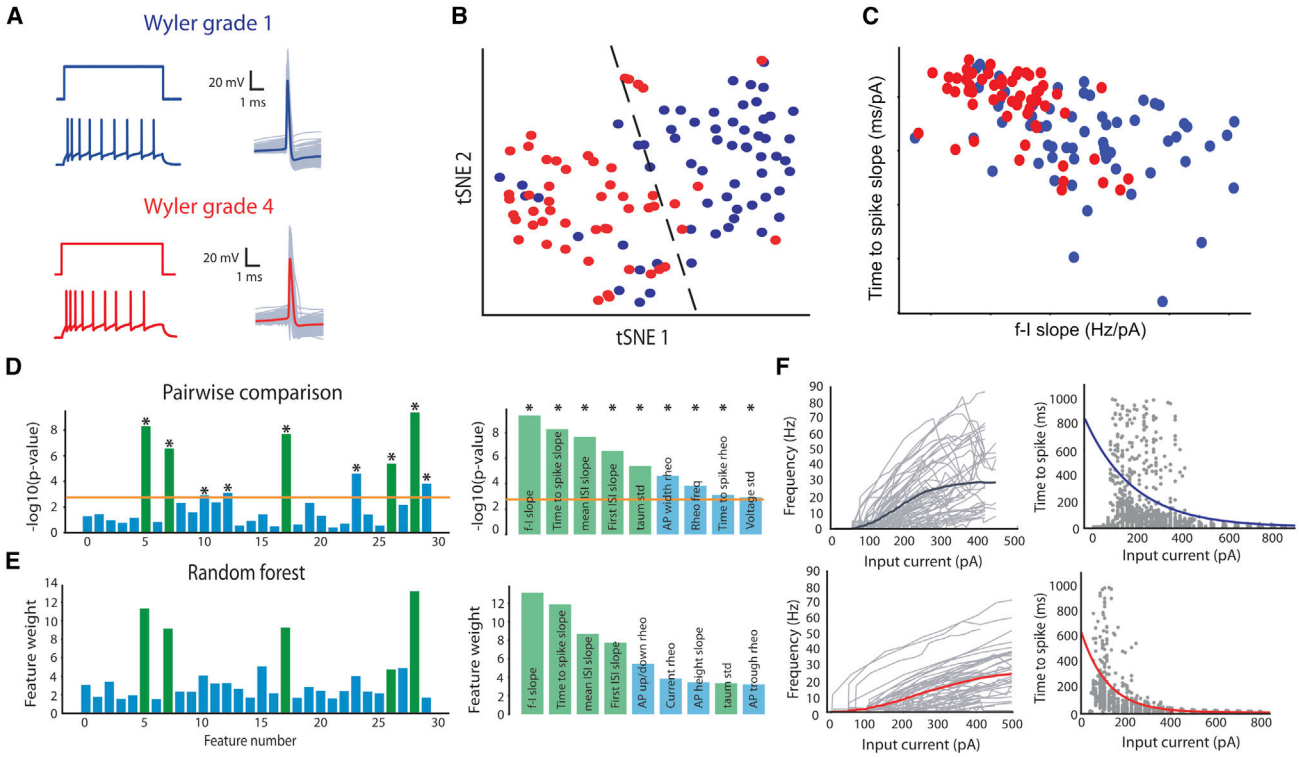

Figure 2. Electrical behavior of human GCs change with disease severity and degree of histological degeneration

(A) Whole-cell patch clamping of DG GCs across patients and somatic spiking responses to 1-s-long dc current injections (blue: WG1; red: WG4). Intracellular somatic spike waveform (thick line: average waveform; thin lines: individual waveforms from a particular experiment).

(B) t-SNE visualization using 31 electrophysiological features from 112 human DG GCs (WG1: 61; WG4: 51 cells; blue: WG1, red: WG4; broken line: k-means decision boundary in t-SNE space between the two main clusters; Table S2).

(C) Two key electrophysiology features leading to WG separation: time-to-spike slope (ms/pA) versus spike-frequency slope (Hz/pA).

(D) Pairwise comparison of electrophysiological features between WG1 and WG4 GCs across feature space (left) and in decreasing levels of statistical significance (right). Statistical significance is calculated using Mann-Whitney U test with the significance level (orange line) Bonferroni corrected for the number of features (*$p < 0.05/30 = 0.002$).

(E) Electrophysiology feature weights of random forest classifier. Shared (green) and non-shared (blue) electrophysiology features between pairwise comparison and random forest classifier among the 10 most influential ones are shown (one out-of-bag validation; classification accuracy = 81%).

(F) Spike frequency and time-to-first-spike response to dc current injections for WG1 (top) versus WG4 (bottom) exhibit altered GC excitability (thick line: average; thin lines: mean response curves from individual experiments; gray points: first spike time in all experimental sweeps).

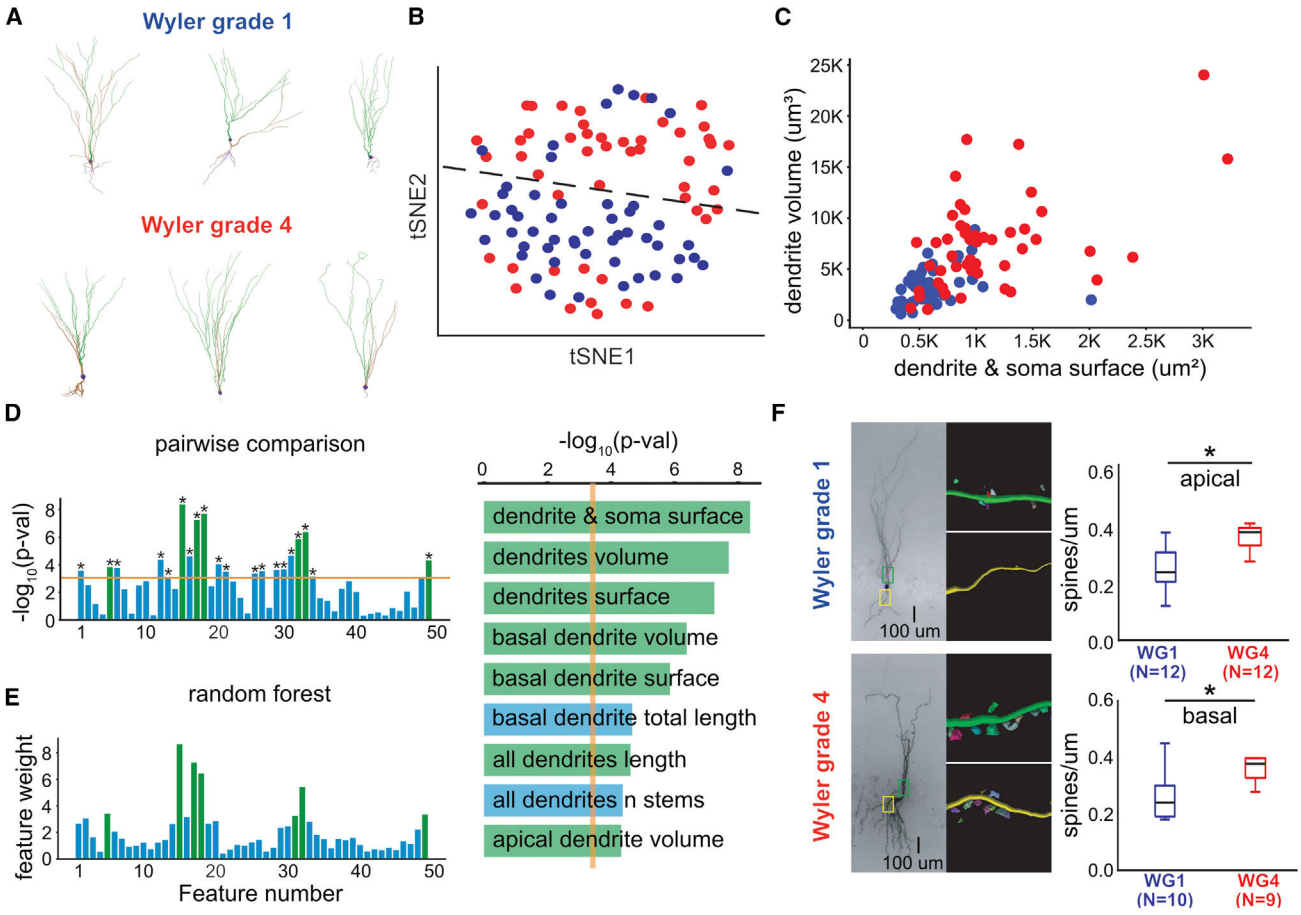

Figure 3. Morphology and spine density of human GCs are affected by disease severity

(A) Reconstructed morphologies of GCs from mild and severe HS donors (green: apical dendrite region; brown: basal dendrite region; violet: axonal region).

(B) t-SNE visualization based on 49 single-cell morphology features of a total of 102 GC reconstructions (see Table S4) illustrates separation (blue: WG1, 52 reconstructions; red: WG4, 50 reconstructions; broken line: k-means clustering).

(C) Two morphology features leading to WG separation: dendritic volume (μm^3) versus dendritic and soma surface area (μm^2).

(D) Pairwise comparison between WG1 and WG4 morphologies (two-sample Mann-Whitney U test, orange line: significance level Bonferroni corrected for the number of features, $p < 0.05/49 = 0.001$).

(E) Weights of the random forest classifier trained solely on morphology features for WG1 and WG4 GCs, out-of-bag classification accuracy 74% (right: features shared between pairwise comparison and random forest classifier shown in green, non-shared ones in blue).

(F) Spine density along human GCs depends on WG. (Left) Morphological reconstructions of single neurons including region-dependent spine density estimation (yellow box: basal region 100 µm after GC layer; green box: apical region 100 µm after GC layer). Individual reconstructed sections with spines along various regions for two WG1 and WG4 neurons are also shown. (Right) Spine density along apical and basal dendrites (boxplots: median,

first and third quartile, and data max/min; significance level = 0.05; p value calculated via Mann-Whitney U test, *$p < 0.05$).

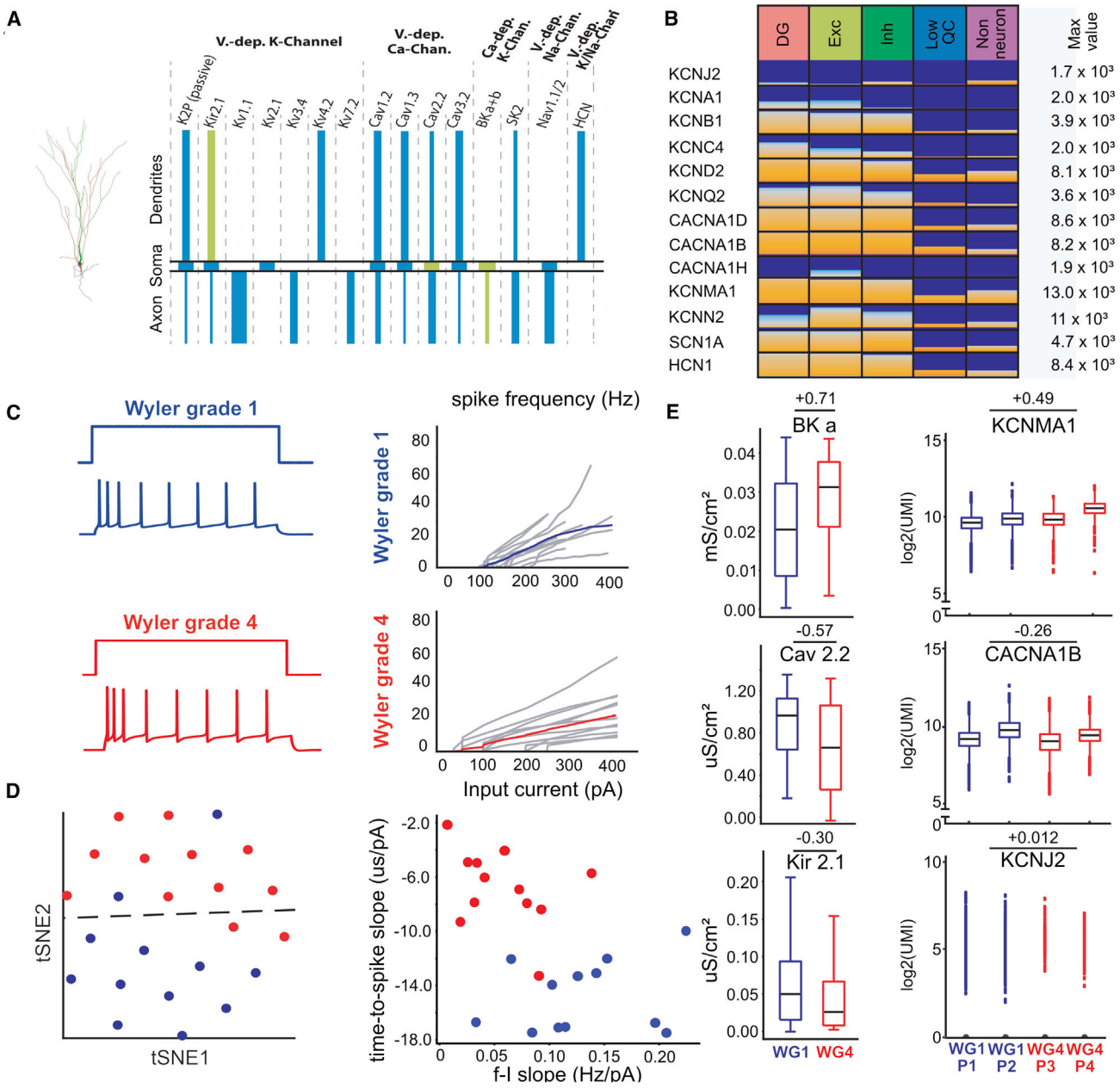

Figure 4. Computational modeling and single-cell RNA sequencing implicate alterations in specific conductances with disease progression

(A) Single-cell model setup using 15 ionic conductances distributed along axonal, somatic, and dendritic sections of the morphology reconstruction. A genetic optimization framework was used to estimate conductance properties (Figure S4) and set parameter values (Table S5) at the single-cell level. Colors indicate ion conductances responsible for model-based WG separation based on conductance values (green: statistically significant differences between WG1 versus WG4 conductances; blue: no statistical significance; p value calculated using Mann-Whitney U test; significance level: $p < 0.05/61 = 0.001$, Bonferroni corrected for multiple comparisons).

(B) Expression profiles of nuclei from human DGs mapped to major cell classes for a subset of genes associated with the ion channels from the GC model setup (A). Columns correspond to different cell classes (left to right): all cells in human DG, excitatory and inhibitory neurons, and non-neuronal cells. Expression levels are shown in CPM base pairs. Colors correspond to the minimal and maximal values of gene expression in the particular cell type. Warmer colors correspond to higher gene expression, and colder colors correspond to lower expression levels. The max value of gene expression is shown on the right for every gene.

(C) Simulated electrophysiological recordings from the GC models resulting from the 3-stage model generation workflow (STAR Methods; see also Figure S4). (Left) GC model responses to 1-s-long dc current injection. (Right) f-I curves from the GC models (thick line: mean; gray lines: individual responses).

(D) t-SNE visualization (left) of the electrophysiology features from the GC models based on their response to 1-s-long somatic dc current injections (blue circles: WG1, red: WG4; left, broken line: k-means clustering). The two most prominent electrophysiology features (right) separating GC models based on WG are the same ones as for experiments (Figures 2C and 2D).

(E) Pairwise comparison of differentially expressed conductances between WG1 and WG4 GCs predicted by the computational models of GCs and 10× snRNA-seq data for BK (KCNMA1), Cav2.2 (CACNA1B), and Kir2.1 (KCNJ2). (Left) For model-based ionic conductance comparisons, the 10 best GC models per cell were chosen (10 models per cell * 12 cells per WG = 120 models per WG; STAR Methods). (Right) Expression profiles of human GCs measured via snRNA-seq from 2 WG1 (blue) and 2 WG4 (red) patients. For BK, Cav2.2, and Kir2.1 (log2 fold change shown; boxes: $25^{th}/75^{th}$ percentile; whiskers: ±1.5× interquartile range). Numbers above the pairwise comparisons show the effect size measured by Cohen’s d. Note that statistical significance could not be estimated using 2 samples per WG.

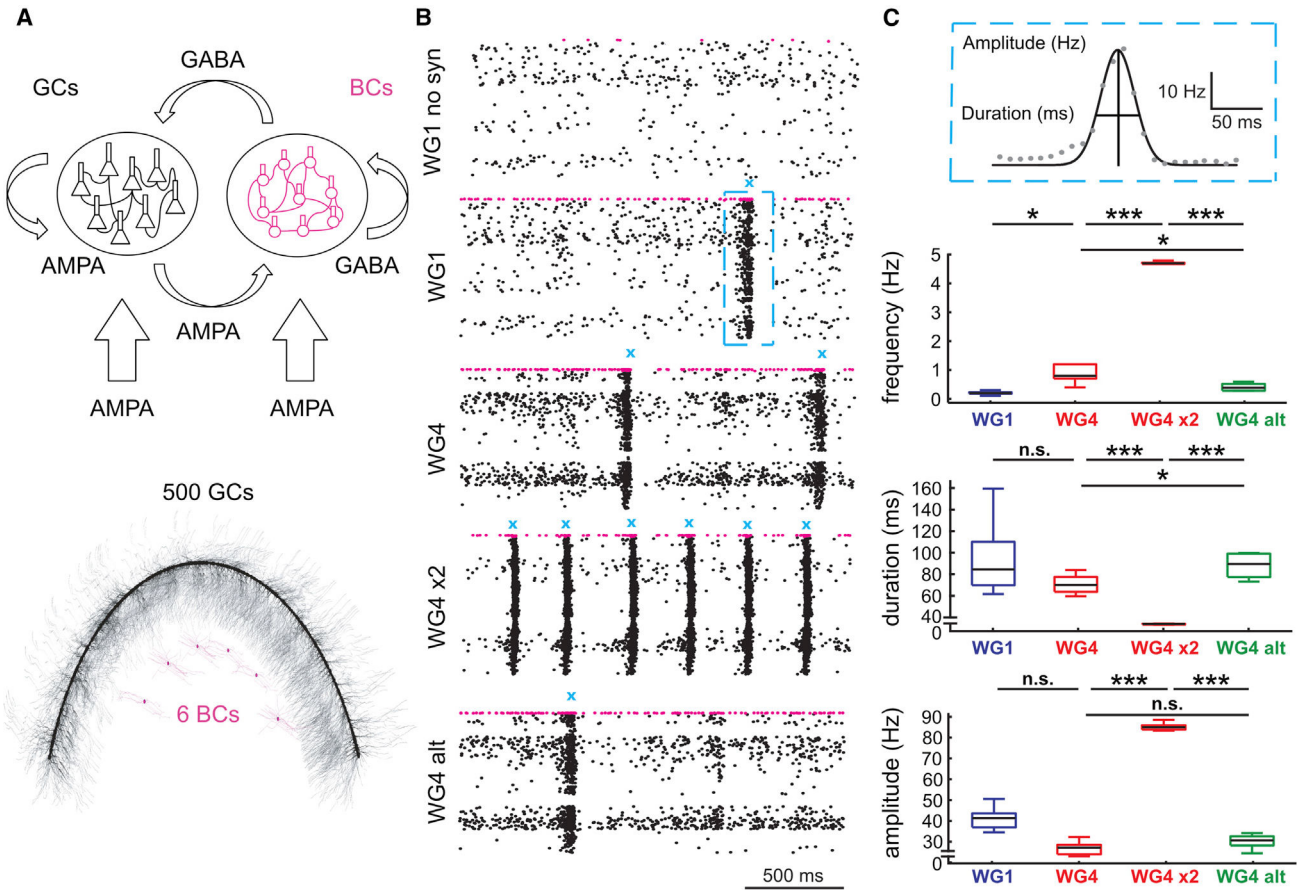

Figure 5. Systematic alterations in GC properties with disease progression reproduce increased pathophysiological excitability in a model of human DG

(A) DG network model consisting of human single-cell models: 500 GCs (black) and 6 BCs (magenta). (Top) Arrows indicate the synaptic connectivity of excitatory (AMPA) and inhibitory (GABA) synapses. Large arrows on the bottom correspond to excitatory synaptic drive from the perforant pathway, and smaller arrows signify within-network synaptic connectivity (see STAR Methods). (Bottom) Morphologically and topographically realistic depiction of the DG network structure.

(B) Raster plots of network dynamics during 2 s of activity driven by perforant path, Poisson-like input (total simulated time: 30 s; black: GC spikes, magenta: BC spikes). (Top to bottom) Unconnected network (only feedforward, “WG1 no syn”); WG1-type network with recurrent connectivity (“WG1”); WG4-type network identical to previous one (“WG1”) but with all WG1 GC models substituted with WG4 GC models (“WG4”); same network as before (“WG4”) but with double the recurrent connectivity between GCs (“WG4 ×2”); and same network as “WG4” but with altered sets of ionic conductances (green in Figure 4A) setting them to their WG1-value (“WG4 alt”). Network dynamics in the presence of recurrent connectivity results in recurrent burst activity (BA; marked in cyan).

(C) Analysis of BA event properties for various DG network configurations. In total, 5 network permutations, each with shuffled connectivity between GCs, were instantiated and simulated for each network configuration. (Top) Definition of three BA event properties: event frequency (i.e., number of BA events per unit of simulated time) and event amplitude

and duration (as defined by fitting a Gaussian envelope to each event; gray: average GC firing rate measured in 10-ms time bins; black: Gaussian fit of BA-event envelope). (Below) BA feature analysis for WG-dependent network configuration (blue: “WG1”; red: “WG4” and “WG4 ×2”; green: “WG4 alt”; line: mean; boxplots: standard error mean across 5 network realizations for each condition). Statistical testing is performed using one-way ANOVA with statistical significance: *$p < 0.05$, **$p < 10^{-3}$, ***$p < 10^{-4}$.

KEY RESOURCES TABLE

REAGENT or RESOURCE	SOURCE	IDENTIFIER
Biological samples		
Single nucleus RNA-sequencing data	This manuscript	https://www.ncbi.nlm.nih.gov/geo/query/acc.cgi?acc=GSE216877
Deposited data		
Single-neuron biophysical all-active models	Allen Institute for Brain Science	https://portal.brain-map.org/explore/models/perisomatic-single-neurons
Data repositories for each figure	Cedars-Sinai and Allen Institute for Brain Science	https://github.com/anastassiou-team/human-epilepsy-project
Software and algorithms		
Python	Python.org	RRID: SCR_008394
Neuron 7.5 Simulator	NEURON	RRID: SCR_005393
scikit-learn: machine learning in Python	http://scikit-learn.org	RRID:SCR_002577
Brain Modeling Toolkit	Allen Institute for Brain Science	https://github.com/AllenInstitute/bmtk
Allen Institute Software Development Kit	Allen Institute for Brain Science	http://github.com/AllenInstitute/AllenSDK
Blue Brain Optimization Toolbox (BluePyOpt)	Blue Brain Project	https://github.com/BlueBrain/BluePyOpt
Electrophys Feature Extraction Library (eFEL)	Blue Brain Project	https://github.com/BlueBrain/eFEL
Neuron Morphology Analysis Toolkit (NeuroM)	Blue Brain Project	https://github.com/BlueBrain/NeuroM
All-active Modeling Workflow	This manuscript	https://github.com/AllenInstitute/All-active-Workflow
Clustering, Classification, RNA-seq data analysis, Simulation, Visualization and All-active Models	This manuscript	https://github.com/AllenInstitute/All-active-Manuscript
Network simulation setup and running	This manuscript	https://github.com/anastassiou-team/human-epilepsy-project/tree/master/Fig_5/network_simulations